

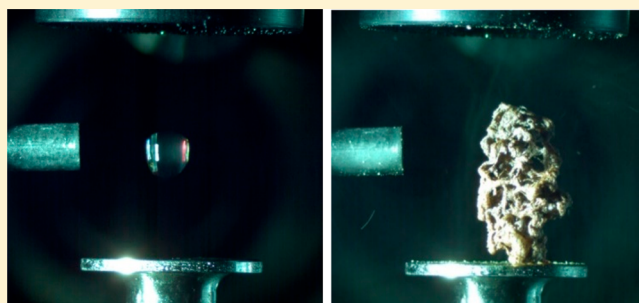
Spectroscopic Study on the Polymer Condensates Formed via Pyrolysis of Levitated Droplets of Dicyanamide-Containing Ionic Liquids

Stephen J. Brotton and Ralf I. Kaiser*

Department of Chemistry, University of Hawaii at Manoa, Honolulu, Hawaii 96822, United States

Supporting Information

ABSTRACT: To investigate the suitability of ionic-liquid-based hypergolic fuels as replacements for traditional hydrazine-based propellants, a 1-methyl-4-amino-1,2,4-triazolium dicyanamide ([MAT][DCA]) droplet, with and without hydrogen-capped boron nanoparticles, was acoustically levitated in argon and heated to successively higher temperatures by a carbon dioxide laser. At each temperature, *in situ* Fourier-transform infrared and near-infrared, Raman, and UV–visible spectra were recorded. The droplet became increasingly yellow before exploding at 400 K to produce a brown foam-like substance and dense smoke. The foam was subsequently studied *ex situ* by X-ray photoelectron spectroscopy, infrared diffuse-reflectance spectroscopy, and elemental analysis. The combined spectroscopic analyses suggest that the foam is formed by linking two or more melamine molecules to yield a combination of melem, melon, and possibly graphitic carbon nitride. At least $37 \pm 3\%$ of the [MAT][DCA] liquid was transformed into the stable, solid-state foam, which would be problematic for the use of such an IL-based hypergolic fuel in rocket engines. 1-Butyl-3-methylimidazolium dicyanamide ([BMIM][DCA]) did not explode and form the foam even at temperatures of up to 430 K. Elimination of the amino group ($-\text{NH}_2$) during the decomposition of $[\text{MAT}]^+$ to volatile products or the increased energy density provided by the additional nitrogen atom in the triazolium ring therefore seem to be required to produce the foam. The present results, provided by an original and accurate experimental technique, elucidate how the nitrogen content affects the stability of an ionic liquid and reveal potential hazards when implementing ionic liquids in bipropellant systems.



1. INTRODUCTION

A hypergolic propellant is composed of a fuel and an oxidizer, which spontaneously ignite upon mutual contact. The most frequently employed hypergolic propellants consist of a dinitrogen tetroxide (N_2O_4) oxidizer and hydrazine (N_2H_4) or its methylated derivatives such as monomethylhydrazine (CH_3NHNH_2) for the fuel.^{1,2} However, hydrazine possesses several disadvantages including extreme toxicity, corrosiveness, flammability, a high vapor pressure, and a relatively low energy density compared to cryogenic propellant combinations such as liquid nitrogen and liquid oxygen.¹ In the past decade, it has been reported that several ionic liquids are hypergolic with common oxidizers^{3–7} such as 1-butyl-3-methylimidazolium dicyanamide ([BMIM][DCA]) and white fuming nitric acid (HNO_3).⁸ An ionic liquid (IL) is a liquid salt consisting of ions and ion pairs that is commonly defined to have a melting point below 373 K.^{9–11} Owing to suitable properties of ionic liquids including a low vapor pressure and high-temperature stabilities, there has been considerable interest in developing ionic-liquid-based hypergolic fuels that are more environmentally friendly, are safer to handle, and have higher energy densities than hydrazine-based propellants.^{3–7} To increase the energy density of the ionic liquids, organic cations have been synthesized with

a high nitrogen content such as imidazolium or triazolium (Scheme 1).¹² Furthermore, dicyanamide anions are often incorporated to produce reduced viscosities and, therefore, lower ignition times (Scheme 1).^{3,13} Another advantage of using ionic liquids is the potential to tune their physical properties such as the melting point, energy density, and viscosity by selecting different anion and cation combinations.^{7,14,15}

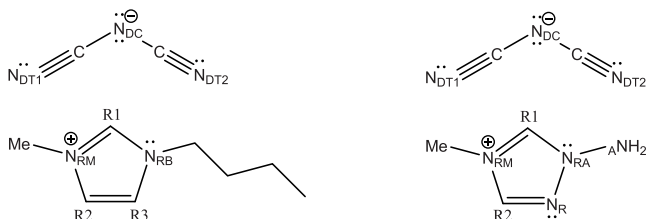
By employing electrospray ionization mass spectrometry, Chingin et al.¹⁶ found that [DCA]-containing ILs react with white fuming nitric acid (WFNA) to produce a precipitate consisting of cyclic triazines including melamine and its polymers melam and melem (Scheme 2). Approximately 25% of the [DCA]-containing IL was transformed into the precipitate following ignition. The production of the precipitate poses at least two problems for employment of the [DCA]-IL and WFNA combination in bipropellant rocket engines.¹⁶ First, the formation of the precipitate during ignition reduces the energy available from the fuel.^{17,18} Second,

Received: September 13, 2018

Revised: December 19, 2018

Published: February 4, 2019

Scheme 1. (Left) Structure of [BMIM][DCA] Showing the [DCA][−] Anion and the Positions of the Methyl (−CH₃) and Butyl (−C₄H₉) Functional Groups on the Imidazolium Ring (C₃N₂H₃); (Right) Structure of [MAT][DCA] Showing the [DCA][−] Anion and the Locations of the Methyl (−CH₃) and Amino (−NH₂) Functional Groups on the Triazolium Ring (C₂N₃H₂)^a

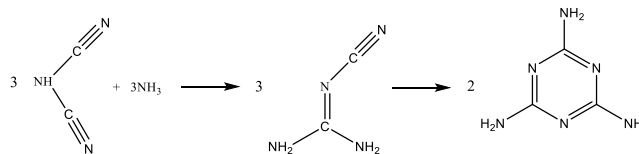


^aThe labelling convention²⁷ for the positions of the nitrogen and carbon atoms in the anion and cations are shown (see section 3.2.4 for further details).

production of a stable solid-state residue within the rocket engine clearly would represent a safety hazard. As shown in Scheme 3, protonated dicyanamide reacts with ammonia (NH₃) to form cyanoguanidine¹⁹ which subsequently polymerizes to yield melamine.²⁰ Chingin et al.¹⁶ therefore concluded that ammonia is required to form melamine in the hypergolic ignition process and suggested the ammonia is produced by the reaction between [DCA][−] and nitric acid. The polymer condensates subsequently form by the thermal condensation of melamine via one of the two pathways proposed in the literature (Scheme 2).²¹ For route (a) shown in Scheme 2, two molecules of melamine first link to form melam with the release of ammonia.²² Melam subsequently condenses to melon^{23,24} and thence to melon accompanied with the production of ammonia at each step. Finally, by losing further ammonia, the melon may condense to graphitic carbon nitride, g-C₃N₄.²⁵ Route (b), also shown in Scheme 2, differs from route (a) only by the exclusion of melam in one of the intermediate steps.

Melamine polymer condensates can be produced from energetic materials by pyrolysis without requirement for an

Scheme 3. Reaction of Protonated Dicyanamide^a with Ammonia To Form Cyanoguanidine, Which Subsequently Polymerizes to Melamine

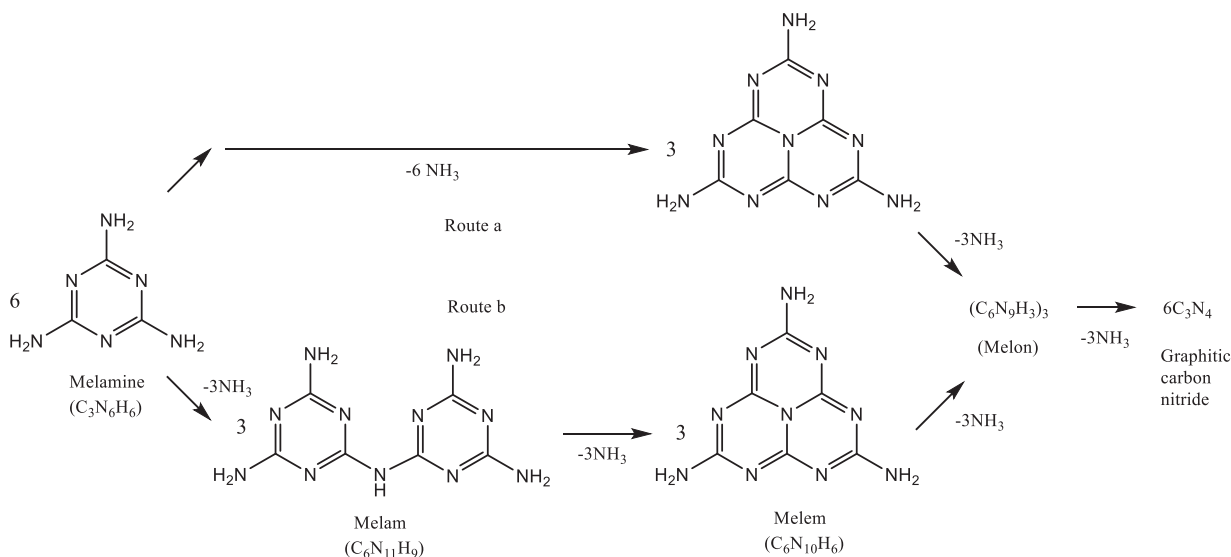


^aThe proton bonded to the central nitrogen of the dicyanamide was previously donated by the HNO₃.¹⁶

oxidizer such as nitric acid. For example, Stoner et al.¹⁷ studied the gases produced by heating energetic materials such as dicyandiamide at the rate of 100 K s^{−1} in argon for pressures up to 5.2 × 10⁴ Torr. Cyclic residues including melamine and melon were found to form in addition to the gases ammonia (NH₃), carbon dioxide (CO₂), hydrogen cyanide (HCN), and nitrous oxide (N₂O). Stoner et al. suggested that the cyclic azines reduce the burn rate in composite propellants by, first, lowering the gas pressure; second, forming on the burning surfaces and thereby lowering the heat and mass transfer; and, third, producing ammonia. Williams et al.¹⁸ reported similar results for a different selection of energetic materials. 1-Ethyl-3-methylimidazolium dicyanamide ([EMIM][DCA]), with its N-containing cation [EMIM]⁺, also condenses to form triazine rings when heated in a nitrogen flow to 773 K and, after further heating to temperatures of up to 1273 K, produces nitrogen-doped graphitic carbon.²⁵

Wooster et al.²⁶ studied the thermal degradation of cyano-containing ionic liquids in a nitrogen atmosphere by temperature-ramped thermogravimetric analysis. ILs with N-containing cations and [DCA][−] anions were found not to completely decompose to volatile products but produced a large mass of charred residue. It was concluded that the “char” only occurred for ILs consisting of N-containing cations and cyano-based anions. Wooster et al.²⁶ suggested that amines (R-NH₂) produced when the N-containing cation decomposes initiate the polymerization of cyano-containing anions.

Scheme 2. Thermal Condensation of Melamine²¹



The temperature at which [DCA]-containing ionic liquids form polymer condensates has been found to depend on the composition of the cation. For example, Perez et al.²⁷ determined the percentage mass change of [MAT][DCA] and [BMIM][DCA] versus temperature in oxygen by thermogravimetric analysis. For [MAT][DCA], as the temperature increased, the mass fraction remained approximately constant until 465 K, after which there was a rapid mass loss of 53%. Thereafter, the remaining mass percentage decreased more gradually between 643 and 853 K toward 1%. Perez et al.²⁷ suggested that the sudden mass loss at 465 K is caused by decomposition of the [MAT]⁺ cation to mostly volatile products, and the substance remaining after [MAT]⁺ decomposed was a polymer derived from [DCA]⁻. The initial decomposition of [BMIM][DCA] occurred more gradually at the higher temperature of 553 K and was analogously attributed to the [BMIM]⁺ cation forming volatile products.

In the present experiments, we used an original apparatus consisting of an ultrasonic levitator enclosed within a pressure-compatible process chamber interfaced to complementary Fourier-transform infrared (FTIR), Raman, and UV–visible spectroscopic probes. Previously, we demonstrated that the apparatus is well suited to study the oxidation of levitated droplets of energetic ionic liquids (EILs).^{28,29} We employ here the same experimental apparatus to investigate spectroscopically the polymer condensates formed by pyrolysis of energetic ionic liquids. The significant advantages of studying the heating of single levitated droplets using the present experimental technique have been discussed in detail^{30,31} (see, in particular, section II F in ref 30). ILs consisting of dicyanamide anions and imidazolium or triazolium cations, such as 1-methyl-4-amino-1,2,4-triazolium dicyanamide ([MAT][DCA]) or [BMIM][DCA], are promising possibilities for the next generation of hypergolic fuels.^{3,5,8,32} However, the production of stable solid-state residues when a [DCA]-containing IL is heated or reacts with the oxidizer clearly poses problems, as discussed above, for implementation in bipropellant engines. We therefore investigate spectroscopically the polymer condensates formed by pyrolysis of [MAT][DCA], and aim to identify the composition of the solid-state residue, measure the temperature at which the rapid polymerization occurs, and determine the fraction of the ionic liquid transformed into the solid. The energy density of EILs can be increased by adding high energy-density solids such as boron.²⁸ The measurements were therefore performed with and without hydrogen-capped boron nanoparticles to investigate the possible effects for the pyrolysis processes. The [BMIM]⁺ cation differs from the [MAT]⁺ cation by having a butyl chain ($-C_4H_9$) rather than an amino functional group ($-NH_2$) and possessing one nitrogen atom fewer in its imidazolium ring (Scheme 1). Considering the importance of nitrogen-containing compounds to initiate the polymerization, such as ammonia¹⁶ or the amines,²⁶ it is highly relevant to determine how the different nitrogen contents of the rings and functional groups of [MAT][DCA] and [BMIM][DCA] affect the polymerization process. Finally, graphitic carbon nitride and the superhard substance β - C_3N_4 are much sought after materials,^{33,34} partly owing to the wide range of potential applications such as optical and electronic engineering, and wear resistant coatings.³⁵ Considering the difficulty in producing β - C_3N_4 ,^{33–36} it is important to investigate alternative possible methods of synthesis such as the pyrolysis of suitable precursors with a high nitrogen content.

2. EXPERIMENTAL METHODS

The levitator experimental apparatus has been reviewed in detail in previous publications.^{29,30} Briefly, the equipment consists of an acoustic levitator,³⁷ operated at the frequency of 58 kHz, enclosed within a pressure-compatible process chamber. The chamber enables levitation in an inert gas, or the introduction of highly reactive gases to study reactions with the droplet. The present experiments were performed in pure argon at a temperature and pressure of 298 K and 880 Torr, respectively. To levitate a droplet with a diameter typically between 1 and 3 mm, a syringe is fixed to the outside port of the process chamber and connected by chemically inert tubing to a microneedle inside the chamber. The needle is attached to the end of a wobble stick and, hence, can be moved to the center of the chamber to levitate the droplet and be withdrawn before the measurements. An ultra-high vacuum (UHV) compatible valve, located between the syringe and the needle, enables the chamber to be sealed after levitating the droplet. The levitated droplet was heated to the required temperatures by adjusting the output power of a 40 W, Synrad Firestar v40 carbon dioxide laser emitting at the wavelength of 10.6 μ m. The temperature of the heated droplet was measured using an FLIR A6703sc thermal imaging camera.

The process chamber is coupled to complementary FTIR, Raman, and UV–visible spectroscopic probes to detect any chemical or physical changes of the processed droplet. In the Raman spectrometer, the 532 nm beam emitted by a diode-pumped, Q-switched Nd:YAG laser is focused by a lens onto the droplet.^{30,38} The Raman-shifted, backscattered photons are subsequently focused by a camera lens into a HoloSpec $f/1.8$ holographic imaging spectrograph and the spectrum recorded by a CCD camera (Princeton Instruments PI-Max 2 ICCD). Two overlaid holographic transmission gratings simultaneously cover the Raman shift ranges of 300–2450 cm^{-1} and 2400–4400 cm^{-1} with a resolution of 9 cm^{-1} . Infrared and near-infrared spectra in the 400–4000 cm^{-1} and 2000–10 000 cm^{-1} wavenumber ranges, respectively, were collected from within a 4 mm diameter volume surrounding the droplet by combining a Thermo Scientific Nicolet 6700 FTIR spectrometer and two stages of mirror optics. For the UV–visible spectrometer, the output from a UV–visible source is transmitted by a fiber-optic feedthrough on a conflat flange to a Y-type reflectance probe inside of the process chamber. The radiation backscattered by the droplet is collected by the read fiber, leaves the chamber via the same conflat fiber-optic feedthrough, and finally enters a StellarNet SILVER-Nova UV–visible spectrometer. The spectrometer operates in the 200–1100 nm wavelength range with a resolution of 2 nm. Hypergolic ignition processes can occur over time scales as short as a few tens of milliseconds.³² To photograph such high-speed events, we installed a Phantom Miro 3a10 camera combined with a Navitar Zoom 6000 modular lens system. The small field of view of the camera-lens system also enables the dimensions of the droplet to be determined precisely.

In addition to the *in situ* spectroscopic techniques discussed above, the processed samples were removed from the chamber and studied by elemental analysis, infrared diffuse-reflectance spectroscopy, and X-ray photoelectron spectroscopy (XPS). First, the percentages by weight of carbon, hydrogen, and nitrogen in the sample were determined by combustion analysis using a PerkinElmer 2400 CHN elemental analyzer. Second, infrared spectra of the samples were recorded by a

diffuse-reflectance accessory (Selector, part number GS19000) installed within the FTIR spectrometer. To permit comparison with the absorption coefficient determined by transmission spectroscopy, the observed diffuse-reflectance spectra of the samples are shown transformed using a Kubelka–Munk function³⁹ in section 3.2.1. Finally, X-ray photoelectron spectra were recorded by an Ulvac PHI Quantera SXM instrument. The sample was ground to a powder and then mounted onto a stainless-steel disc before analysis. A monochromatized Al K α source supplied photons with an energy of 1486.6 eV across an area of 1.4 mm \times 0.3 mm. The energies of the photoelectrons ejected from the sample at an angle of 45° were measured by an electron energy analyzer. The pass energy for the electron energy analyzer was 26 eV, which results in an energy resolution of approximately 1.7 eV full-width at half-maximum. The electron energy scale was calibrated using the C(1s) peak of adventitious carbon at 284.8 eV,⁴⁰ and hence the possible shifts produced by charging effects were removed.

The [MAT][DCA] was synthesized as described by Hawkins et al.⁴¹ The [MAT][DCA]-capped hydrogen-terminated boron nanoparticles were prepared according to the procedure discussed in ref 42. The boron-doped [MAT][DCA] was made by mixing 5% by weight of the boron nanoparticles with the pure ionic liquid.

3. RESULTS AND DISCUSSION

3.1. Heating the Levitated [MAT][DCA] Droplet. The duty cycle of the carbon dioxide laser was increased from 3% to 8% in increments of 1% and the droplet irradiated for 10 min at each step. The temperature of the droplet was measured at each duty cycle by the IR thermal imaging camera. Fourier-transform infrared, Fourier-transform near-infrared, Raman, and UV–visible spectra in addition to photographs were recorded at room temperature before heating and at each successively higher temperature. Photographs of the droplets of [MAT][DCA] and boron-doped [MAT][DCA] levitated in argon when heated from 298 to 400 K are shown in Figure 1. The unheated [MAT][DCA] droplet is a spheroid with horizontal, h , and vertical, v , diameters of $h = 2.9 \pm 0.1$ mm and $v = 3.1 \pm 0.1$ mm, and $h = 2.9 \pm 0.1$ mm and $v = 1.7 \pm 0.1$ mm for the unheated boron-doped sample. The [MAT][DCA] droplet became increasingly yellow before exploding at 400 K to form a brown foam-like substance and filling the chamber with a dense smoke. For the droplet containing boron nanoparticles, yellow bubble-like structures appeared beneath the surface prior to the explosion. By measuring the dimensions of a droplet using the visible camera (section 2), using 1.277 g cm^{-3} for the density of [MAT][DCA],⁷ and removing the foam from the process chamber to be weighed, we determined that $37 \pm 3\%$ (by weight) of the ionic liquid was transformed into the foam. Since the smoke is likely composed of fine particles of the foam (section 3.2.2), the value of 37% is a lower limit. In contrast to [MAT][DCA], we found that [BMIM][DCA] does not explode to form the brown foam at 400 K or even at higher temperatures of up to 433 K.

3.2. Composition of the Heating Products. In this section, the different spectroscopic techniques discussed in section 2 are used to identify the composition of the foam and smoke. Infrared (IR) spectroscopy rarely permits identification of specific complex organic molecules, but IR spectroscopy is a powerful approach to identify any new functional groups formed. The foam is opaque and hence best studied *ex situ* by



Figure 1. Photographs of droplets of [MAT][DCA] (left column) and boron-doped [MAT][DCA] (right column) heated by a carbon dioxide laser from room temperature (298 K) to 389 and 400 K. The droplets became increasingly yellow before exploding to form a brown foam-like substance at 400 K.

diffuse-reflectance infrared spectroscopy (section 3.2.1), whereas the smoke must be examined *in situ* within the chamber using the combined FTIR spectrometer and mirror system operated in transmission mode (section 3.2.2). Raman scattering provides information complementary to infrared absorption spectroscopy about the rovibrational modes of molecules (section 3.2.3). In particular, a Raman transition does not require a permanent electric dipole moment, and so Raman lines are observed for symmetric molecules. UV–visible spectroscopy enables investigation of electronic transitions and, of particular relevance here, determination of whether the sample has polymerized because of the heating (section 3.2.3). X-ray absorption spectroscopy provides information regarding the chemical environment of the atom emitting the radiation and, hence, can identify chemical states such as C=N–C, C–N=H₂, and N₂=C=N present in the polymer condensates (section 3.2.4). Finally, elemental analysis gives molar ratios including N/C and so can discern between the different polymer condensates of melamine, namely, melam, melem, melon, and graphitic carbon nitride (section 3.2.5). Combining the above complementary and distinct spectroscopic techniques into a single coherent picture is a powerful approach to identify the product molecules formed. In section 3.3, we discuss a remarkable phenomenon, not related to identifying the heating products, in which the

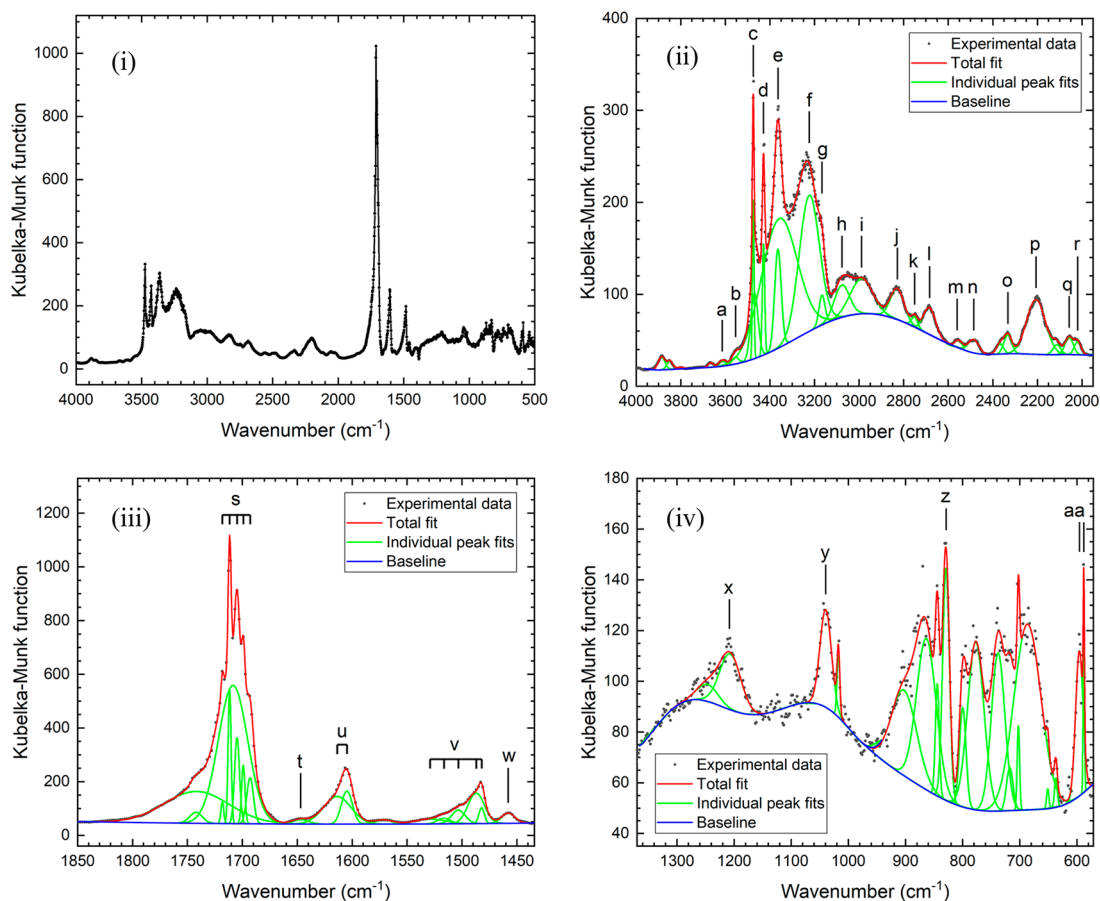


Figure 2. Infrared diffuse-reflectance spectra of melamine. The spectrum for the full wavenumber range is shown in (i) and the individual peak fits are presented in (ii), (iii), and (iv). The vibrational assignments for the peaks labeled a–aa are given in Table 1.

near-infrared beam appears to pass through the levitated droplet without significant deflection to record undistorted absorption lines.

3.2.1. Infrared Diffuse-Reflectance Spectroscopy of the [MAT][DCA] Foam. As a guide to interpreting the infrared spectrum of the [MAT][DCA] foam, we first studied the infrared spectrum of melamine. The infrared diffuse-reflectance spectrum of melamine is shown in Figure 2 together with the curve fits to decompose the spectrum into the component peaks. The best-fit wavenumbers and vibrational mode assignments for the individual peaks a–aa are presented in Table 1. The fundamental modes were assigned by comparison with the measurements and theoretical calculations of Yuan et al.⁴³ for crystalline melamine. The infrared spectrum of melamine has been studied by other authors in both the gas phase⁴⁴ and crystalline form.⁴⁵ The present peak wavenumbers correspond to the values in ref 43 with sufficient accuracy to permit clear assignments in most spectral regions. For the present measurements, however, peaks s, u, and v are split into several very narrow peaks that extend to higher wavenumbers than the corresponding peaks in ref 43, perhaps because of differences in the molecular geometry and intermolecular hydrogen-bonding environments for the two samples studied. The different types of vibrational modes of melamine generally occur in different spectral regions. According to normal coordinate analysis, the N–H stretching modes occur in the 3100–3650 cm^{-1} region, the C–N ring modes are prominent from 1100 to 1700 cm^{-1} , and the peaks around 814 cm^{-1} are produced by the N–H or C–N bending modes. However, the

actual description is more complicated, as shown in Table 1, because of coupling between the different vibrational modes.

The infrared diffuse-reflectance spectrum of the [MAT][DCA] foam is shown in Figure 3 together with fits to the individual peaks a–aa. The wavenumbers and vibrational mode assignments for peaks a–aa are presented in Table 2. The assignments were performed by comparison with the vibrational modes of melamine from Table 1 and [MAT][DCA].²⁸ A comparison of the full-range spectra for melamine (Figure 2i) and the [MAT][DCA] foam (Figure 3i) reveals similarities in the overall shape and main features. For example, the broad rise that starts at approximately 3700 cm^{-1} , reaches a maximum near 3350 cm^{-1} , and then gradually decreases as the wavenumber reduces to 2000 cm^{-1} . Also, the largest peaks in the [MAT][DCA] foam and melamine spectra occur at similar wavenumbers, that is, 1712 and 1699 cm^{-1} , respectively. Furthermore, peak y at 813 cm^{-1} in the foam spectrum clearly corresponds to peak z in the melamine spectra at 829 cm^{-1} and the 814 cm^{-1} peak in ref 43. However, many of the sharper features in the melamine spectra (Figure 2), such as peaks c–e produced by N–H stretches and peaks u and v assigned to the C–N modes, are not clearly evident in the [MAT][DCA] foam. A similar loss of sharp structure occurs in the FTIR spectra when melamine thermally condenses to melem.²² By fitting to the [MAT][DCA] foam spectra, it is nevertheless possible to decompose the almost shapeless structure into many of the same peaks as present in melamine. For example, by fitting to the indistinct shoulders and peaks in the region from 3700 to 3300 cm^{-1} it is possible

Table 1. Wavenumbers and Vibrational Mode Assignments for the Observed Peaks in the Infrared Diffuse-Reflectance Spectrum of Melamine^a

peak label ^b	present measured wavenumbers (cm ⁻¹) ^c	reference measured wavenumbers ⁴³ (cm ⁻¹)	reference theoretical wavenumbers ⁴³ (cm ⁻¹)	vibrational mode assignment
a	3614			possible 3 x combination mode
b	3554			possible 2 v + aa combination mode
c	3475	3468	3555	N—H bond asym. stretch vib.
d	3429	3420	3494	N—H bond asym. stretch vib.
e	3364	3331	3393	N—H bond asym. stretch vib.
			3370	
f	3224		3221	N—H bond sym. stretch vib.
g	3166	3129	3170	N—H bond sym. stretch vib.
h	3077 ± 4			u + v combination mode
i	2989 ± 6			2 v combination mode
j	2828			u + x combination mode
k	2751			s + y combination mode
l	2684			v + x combination mode
m	2553			very weak
n	2486			3 z combination mode
o	2333 ± 2			v + z combination mode
p	2206			t + aa combination mode
q	2058 ± 2			v + aa combination mode
r	2019 ± 3			z + x combination mode
s	1718	1650	1651	N—H bond in-plane bend and shear vib.
	1712			
	1705			
	1699			
	1693			
t	1647			2 z combination mode
u	1614	1548	1549	N—H in-plane bend and rock vib. + in-plane bend vib. of out-of-ring C—N + stretch vib. of out-of-ring C—N + stretch vib. of in-ring C—N bond
	1605			
v	1529 ± 21	1469	1462	N—H bond in-plane rock, bend and sym. stretch vib. + in-plane bend vib. of out-of-ring C—N + stretch vib. of out-of-ring C—N + stretch vib. of in-ring C—N bond
	1516 ± 10	1438	1435	
	1503 ± 3			
	1487 ± 3			
	1482			
w	1458			
x	1207 ± 6	1195	1190	N—H bond in-plane bend and rock vib.
y	1040	1026	1031	N—H bond in-plane bend and rock vib.
z	829	814	850–500	N—H bond out-of-plane bend vib. + out-of-plane bend vib. of out-of-ring C—N + out-of-plane bend vib. in-ring C—N
aa	588	582	850–500	same assignment as peak z

^aThe assignments of the fundamental modes were performed by comparison with the theoretical calculations and measurements of ref 43. ^ba–aa correspond to the peak labels in Figure 2. ^cThe quoted errors combine the uncertainties from determining the peak wavenumbers in the fitting procedure and calibrating the wavenumber scale. The uncertainties are equal to, or less than, 1 cm⁻¹ unless stated otherwise.

to extract peaks b–e associated with the N—H stretches. The best-fit peak wavenumbers of the foam and melamine are compared in Table 2, which reveals a clear similarity between the wavenumbers for peaks a–e, l–q, and y–aa in the foam spectrum and wavenumbers for the corresponding peaks in melamine. Therefore, in Table 2, peaks a–e, l–q, and y–aa are assigned to the same vibrational modes as the peaks in the melamine spectrum with similar wavenumbers. There are, however, several features in the foam spectrum not present in the melamine spectrum. In particular, peaks i–k at 2228, 2192, and 2133 cm⁻¹, which are attributed to the $\nu_s(\text{C—N}) + \nu_{as}(\text{C—N})$ combination band, the $\nu_s(\text{C}\equiv\text{N})$ symmetric stretching mode, and the $\nu_{as}(\text{C}\equiv\text{N})$ asymmetric stretching mode of dicyanamide, respectively.^{46,47} Also, the very small peaks r–x have similar wavenumbers as some of the

[MAT][DCA] modes studied in ref 28 and so are assigned in Table 2 to small quantities of the unreacted ionic liquid.

In summary, the similar wavenumbers for many of the peaks in the foam and melamine spectra suggests that the two substances share the same functional groups. FTIR spectroscopy does not, however, enable clear identification of the specific polymer formed (see Scheme 2). Several minor features in the [MAT][DCA] foam spectrum not present in melamine indicate that small quantities of unreacted [MAT][DCA] remain.

3.2.2. In Situ Infrared Absorption Spectroscopy of the Smoke. Infrared absorption spectra of [MAT][DCA] levitated in argon are shown in Figure 4 as the droplet is heated to successively higher temperatures by the carbon dioxide laser. When the temperature is increased from 298 to 389 K, there are no significant changes in the FTIR spectra. The only

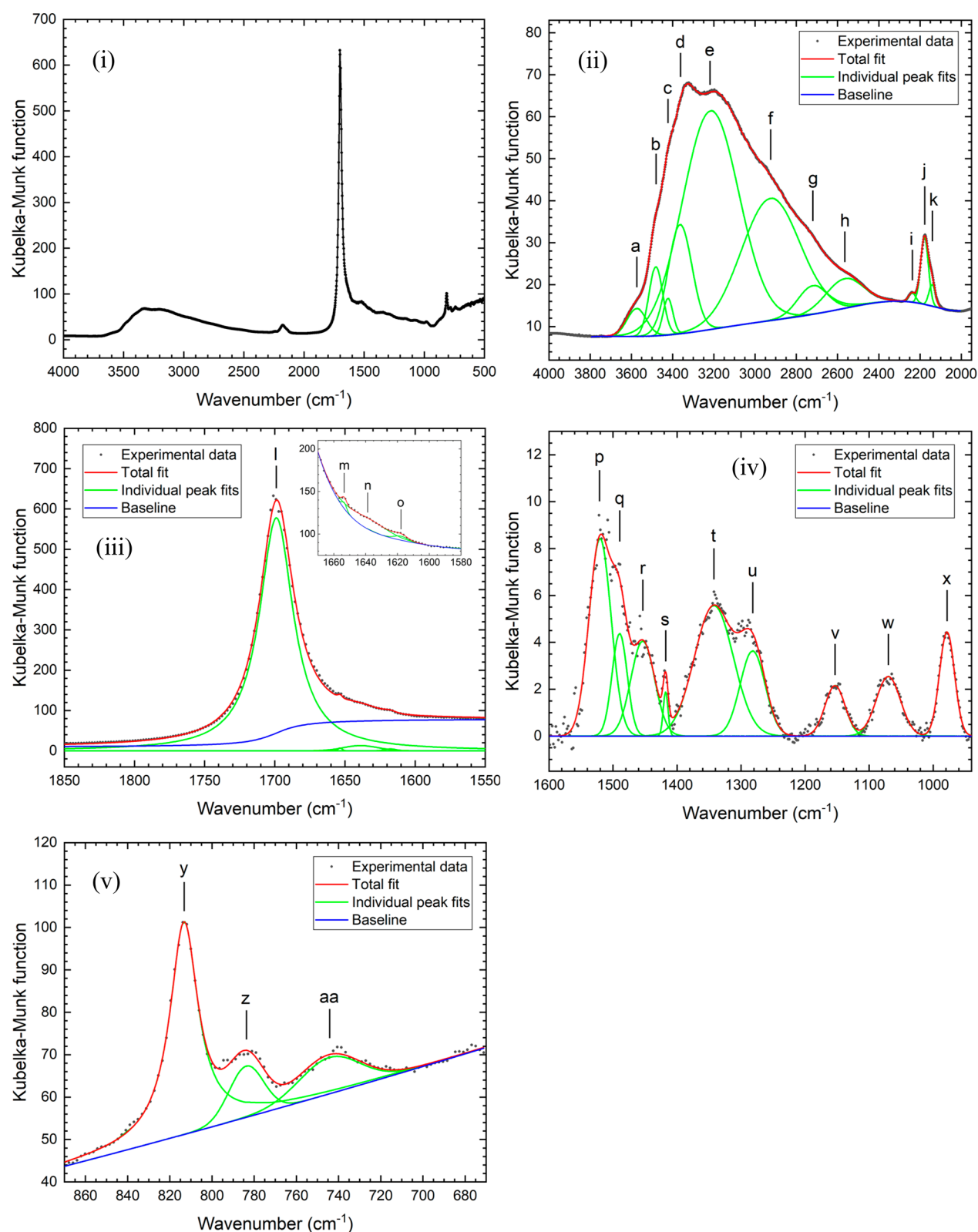


Figure 3. Infrared diffuse-reflectance spectra of the [MAT][DCA] foam. The spectrum for the full wavenumber range is shown in (i) and the individual peak fits are presented in (ii) to (v). The vibrational mode assignments for the peaks labeled a–aa are given in Table 2. A background has been subtracted from the spectrum in (iv) to display the very small structure with increased amplitude.

observable structure consists of oscillations at wavenumbers below approximately 1300 cm^{-1} produced by scattering from the droplet.^{48,49} However, following production of the foam at 400 K, a large “dispersion artefact” appears at 1706 cm^{-1} with a

derivative-like lineshape caused by scattering of the infrared beam from the smoke particles. Fits to the individual lineshapes a–i in the infrared absorption spectrum of the smoke are presented in Figure 5. The wavenumbers and

Table 2. Wavenumbers and Vibrational Mode Assignments for the Observed Peaks in the Infrared Diffuse-Reflectance Spectrum of the [MAT][DCA] Foam^a

peak label ^b	foam peak wavenumber (cm ⁻¹) ^c	melamine peak wavenumber (cm ⁻¹)	[MAT][DCA] peak wavenumber ²⁸ (cm ⁻¹)	vibrational mode assignment
a	3574 ± 2	3614		combination modes (see Table 1)
b	3480	3475		N—H bond asym. stretch vib.
c	3423	3429		N—H bond asym. stretch vib.
d	3363	3364		N—H bond asym. stretch vib.
e	3216 ± 5	3224		N—H bond sym. stretch vib.
i	2237		2228	Fermi enhanced $\nu_s(\text{N—C}) + \nu_{as}(\text{N—C})$ combination band
j	2177		2192	$\nu_s(\text{C}\equiv\text{N})$ (A ₁)
k	2140		2133	$\nu_{as}(\text{C}\equiv\text{N})$ (B ₂)
l	1699	1712		N—H bond in-plane bend and shear vib.
m	1654	1647		combination mode (see Table 1)
n	1639	1614		N—H in-plane bend and rock vib. + in-plane bend vib. of out-of-ring C—N + stretch vib. of out-of-ring C—N + stretch vib. of in-ring C—N bond
o	1618 ± 3	1605		
p		1529 ± 21		N—H bond in-plane rock, bend and sym. stretch vib. + in-plane bend vib. of out-of-ring C—N + stretch vib. of out-of-ring C—N + stretch vib. of in-ring C—N bond
		1520 ± 2		
		1516 ± 10		
		1503 ± 3		
q	1490 ± 2	1487 ± 3		
		1482		
r	1454 ± 3	1458		
r	1454 ± 3		1455	ν_{39} N(2)—C(3) and N(4)—C(5) sym. stretch very weak
s	1418 ± 1			
t	1342 ± 2		1310	ν_7^*
u	1282 ± 2			C—N—C asym. stretch of [DCA] ⁻
v	1153 ± 1		1171	ν_{30} C(5)—H wag + N(1)—CH ₃ stretch
w	1070		1071	ν_{27} ring C—N—C sym. stretch + C(5)—H wag and CH ₃ rock
x	978		978	ν_{26} N(1)—N(2) stretch + C(3)—H in-plane wag
y	813	829		N—H bond out-of-plane bend vib. + out-of-plane bend vib. of out-of-ring C—N + out-of-plane bend vib. in-ring C—N
z	784			
aa	744			

^aThe assignments were performed by comparison with the vibrational modes of melamine in Table 1 and [MAT][DCA] from ref 28. ^ba–aa correspond to the peak labels in Figure 3. ^cThe quoted errors combine the uncertainties from determining the peak wavenumbers in the fitting procedure and calibrating the wavenumber scale. The uncertainties are equal to, or less than, 1 cm⁻¹ unless stated otherwise.

vibrational mode assignments for lineshapes a–i are presented in Table 3. In order to interpret the spectra, it is necessary to account for the absorption and scattering of light by small particles. The interaction between electromagnetic radiation and a dielectric particle with dimensions comparable to the wavelength results in Mie scattering.⁴⁸ Nonresonant Mie scattering causes broad sinusoidal-like oscillations across the baseline of FTIR spectra. In contrast, resonant Mie scattering arises when the wavenumber passes through an absorption band. Consequently, absorption lines have an asymmetric shape, and a sharp decrease is observed on the high-wavenumber side of the band.⁴⁹ Both nonresonant and resonant Mie scattering can significantly alter the position, intensity, and shape of an absorption line, which makes retrieving the undistorted spectrum challenging. The spectrum in Figure 5 is clearly significantly distorted by the scattering of the infrared beam from the smoke particles. To account for resonant Mie scattering, for modes h and i asymmetric profiles were optimized in the fitting procedure of the Shore form:⁵⁰

$$\text{absorbance} = C(\tilde{\nu}) + \frac{(\Gamma/2)B + (\tilde{\nu} - \tilde{\nu}_0)A}{(\tilde{\nu} - \tilde{\nu}_0)^2 + (\Gamma/2)^2} \quad (1)$$

where $C(\tilde{\nu})$ is a background that varies slowly with the wavenumber $\tilde{\nu}$ ($=1/\lambda$), $\tilde{\nu}_0$ is the peak wavenumber, Γ is the resonance width, and A and B are proportional to the asymmetric and symmetric amplitudes, respectively. To account for baseline oscillations in the high-shift regions produced by nonresonant Mie scattering, a sinusoidal term of the form $D \sin(kx + \Delta)$ with variable amplitude, D , wavenumber, k ($=2\pi/\lambda$), and phase, Δ , was included in the fitting function. The resulting resonance wavenumbers $\tilde{\nu}_0$ for lineshape h at 1706 cm⁻¹ and lineshape i at 816 cm⁻¹ are close to the values of 1699 and 813 cm⁻¹, respectively, for the foam (see Table 3). Therefore, mode h is assigned to the N—H bend and shear vibration, and mode i to the out-of-plane bending vibrations of the N—H and C—N bonds. After accounting for the oscillatory background, it becomes possible to fit to the broad, distorted structure between 3600 and 2300 cm⁻¹ and thereby assign the retrieved symmetric peaks a to d to N—H stretches (Table 3). The undistorted peaks e, f, and g at 2233,

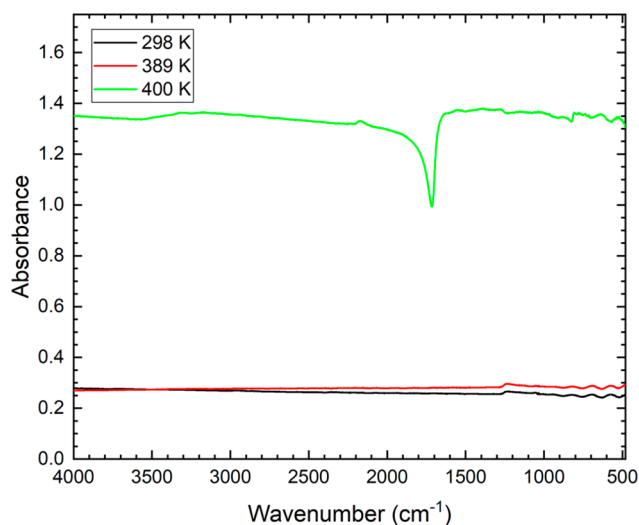


Figure 4. Infrared absorption spectra of boron-doped [MAT][DCA] levitated in argon as the droplet is heated to successively higher temperatures by the carbon dioxide laser. The curve corresponding to 400 K is the spectrum of the smoke produced following formation of the [MAT][DCA] foam. The curve fits to decompose the 400 K spectrum into its component peaks are presented in Figure 5.

2176, and 2140 cm^{-1} are produced by vibrational modes of the $[\text{DCA}]^-$ anion.^{46,47} The remainder of the spectrum is too distorted by scattering effects to permit further information to be extracted by the present technique. In our analysis, the unlabeled, fitted peaks in Figure 5 are therefore effectively a background for lineshapes a to i. Thus, by accounting for scattering effects, we have analyzed some spectral regions of the absorption spectrum shown in Figure 5 and shown that the foam and smoke particles appear to be composed of the same substance.

3.2.3. In Situ UV–Visible and Raman Spectroscopies. The UV–visible reflectance spectra in the 200–1100 nm wavelength range of [MAT][DCA] levitated in argon as the droplet is heated to successively higher temperatures are shown in Figure 6. Clearly, the heating generally causes the absorption ($\propto 1 - \text{reflectance}$) in the UV region to increase relative to that in the optical and near-infrared ranges, and the absorption maximum to extend to longer wavelengths. It is well established that conjugated π -electron systems involving double bonds, such as $\text{N}_2=\text{C}=\text{N}$ (Scheme 2), absorb in the UV spectral region, and each additional double bond causes the absorption maxima for the $\pi \rightarrow \pi^*$ excitations to shift to longer wavelengths.⁵¹ The spectra in Figure 6 therefore suggest that heating produced an increase in the number of conjugated double bonds, which is consistent with polymerization. For the boron-doped [MAT][DCA], the boron nanoparticles cause the ionic liquid to blacken, and therefore the region of high absorption extends across the full wavelength range. Aside from a small increase in the reflectance at longer wavelengths, there are no noteworthy changes in the UV–visible spectra between 298 and 389 K. In contrast, after production of the foam, the spectrum changes dramatically to resemble the foam spectrum without the boron. To summarize, UV–visible spectroscopy suggests that the [MAT][DCA] has polymerized because of the heating, which would be consistent with either condensation pathway in Scheme 2.

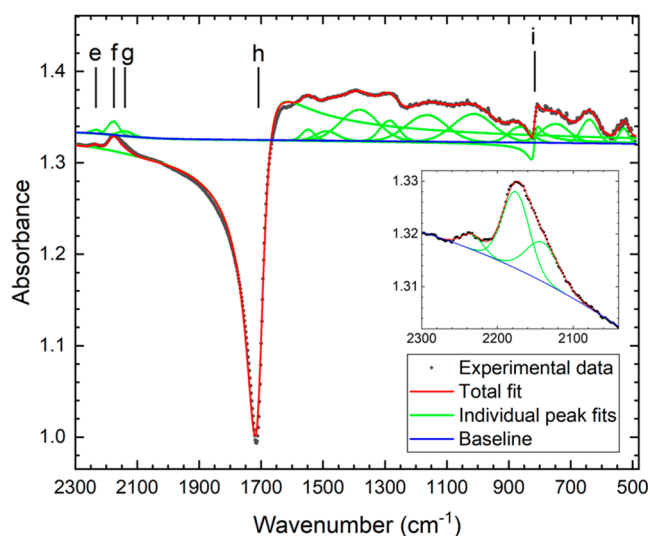
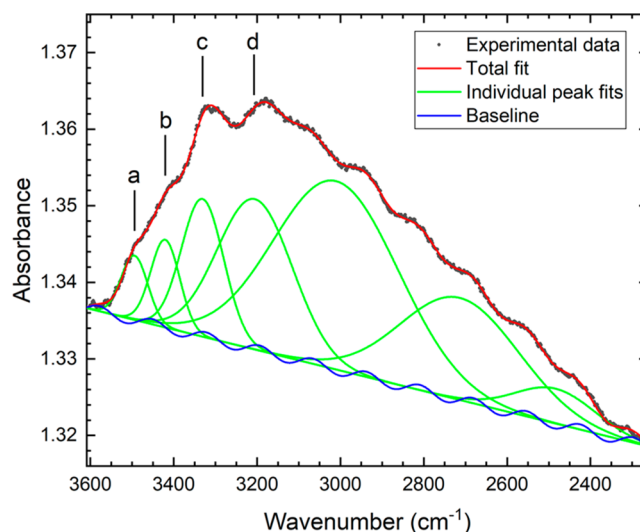


Figure 5. Individual peak fits to the infrared absorption spectrum of the smoke produced following formation of the [MAT][DCA] foam (see the 400 K curve in Figure 4). To account for scattering effects, asymmetric profiles for modes h and i and an oscillatory baseline were optimized in the fitting procedure. Vibrational assignments for the peaks labeled a–i are given in Table 3.

The Raman spectra of [MAT][DCA], with or without boron nanoparticles, levitated in argon as the droplet was heated to successively higher temperatures are shown in Figure 7. Thus, the heating caused the peaks to vanish and produced large fluorescent backgrounds, so that no information could be extracted about the chemical changes.

3.2.4. X-ray Photoelectron Spectroscopy of the [MAT][DCA] Foam. The X-ray photoelectron spectrum of the [MAT][DCA] foam in the N(1s) spectral region is shown in Figure 8 together with fits to the individual peaks labeled a–c. The binding energies and relative areas for peaks a–c are presented in Table 4. To model the step-like, slow onset of the continuum, the background was represented by a broadened, arctangent function in the fitting procedure.⁵² As shown in Scheme 1, there are seven chemical environments for the nitrogen atoms in [MAT][DCA], namely, N_{RM} , N_{RA} , N_{R} , N_{A} , N_{DC} , N_{DT1} , and N_{DT2} . Perez et al.²⁷ measured the experimental

Table 3. Wavenumbers and Vibrational Mode Assignments for the Peaks in the Infrared Absorption Spectrum of the Smoke Compared with the Peak Wavenumbers of the Foam Spectra from Table 2

peak label ^a	foam-smoke peak wavenumber ^b (cm ⁻¹)	foam peak wavenumber ^b (cm ⁻¹)	vibrational mode assignment
a	3494 ± 2	3480	asym. NH ₂ stretch
b	3420	3423	asym. NH ₂ stretch
c	3331 ± 2	3363	asym. NH ₂ stretch
d	3205 ± 3	3216 ± 5	sym. NH ₂ stretch
e	2233	2237	Fermi enhanced $\nu_s(\text{N}-\text{C}) + \nu_{\text{as}}(\text{N}-\text{C})$ combination band
f	2176	2177	$\nu_s(\text{C}\equiv\text{N})$ (A ₁)
g	2140	2140	$\nu_{\text{as}}(\text{C}\equiv\text{N})$ (B ₂)
h	1706	1699	N—H bond in-plane bend and shear vibration
i	816 ± 2	813	N—H bond out-of-plane bend vib. + out-of-ring C—N bond bend. vib. + in-ring C—N bond bend. vib.

^aa–i correspond to the peak labels in Figure 5. ^bThe quoted errors combine the uncertainties from determining the peak wavenumbers in the fitting procedure and calibrating the wavenumber scale. The uncertainties are equal to, or less than, 1 cm⁻¹ unless stated otherwise.

binding energies and calculated the core energies for the seven chemical environments. Owing to small differences in the binding energies for N_{RM} and N_{RA} (402.3 and 402.1 eV), N_R and N_A (400.5 and 400.5 eV), and N_{DT1} and N_{DT2} (397.9 and 397.7 eV), the observed XPS spectrum of [MAT][DCA] appears as four peaks spanning the binding energy range from approximately 396.2 to 403.8 eV. The [MAT][DCA] spectrum is thus dissimilar to the N(1s) XPS spectrum in Figure 8 and, hence, [MAT][DCA] is not a major constituent of the foam.

We next compare the N(1s) spectrum in Figure 8 with the corresponding XPS spectrum of melamine. As Schemes 2 and 3 show, there are two chemical environments for the nitrogen atoms in melamine, namely, C=N—C and C—N=H₂. The experimental N(1s) XPS spectrum of melamine is composed of three peaks at 398.5, 399.1, and 400.7 eV.⁵³ The peaks at 398.5 and 399.1 eV were assigned to the C—N=H₂ and C=N—C chemical states, respectively. By comparison with the XPS spectrum of aniline,⁵⁴ the remaining peak at 400.7 eV was tentatively attributed to a second chemical state for the amino-nitrogen atom, C=N⁺=H₂ (Table 4). As Table 4 shows, the binding energies of peaks a–c at 398.7, 399.1, and 400.7 eV, respectively, for the [MAT][DCA] foam coincide closely with the values for melamine. Furthermore, the overall shapes of the XPS spectra for the foam and melamine are similar. Thus, N(1s) XPS spectroscopy suggests that the nitrogen atoms reside in essentially the same chemical states in melamine and the foam. Further significant information can be deduced from the observation that the relative areas of the peaks differ in the foam and melamine. In the XPS spectra of melamine, the ratio of the peak areas corresponding to the C=N—C and C—N=H₂ chemical states is 1:1,⁵³ which is consistent with the relative number of these two chemical states in the molecule. In contrast, the ratio of the C=N—C to C—N=H₂ peak areas in the present measurements is 3.3 ± 1.8. When melamine polymerizes to melam, melem, melon, and finally β -C₃N₄ (see Scheme 2), the relative number of C=N—C to C—N=H₂ bonds increases as 1, 3/2, 2^{1/3}, 7, and ∞ .

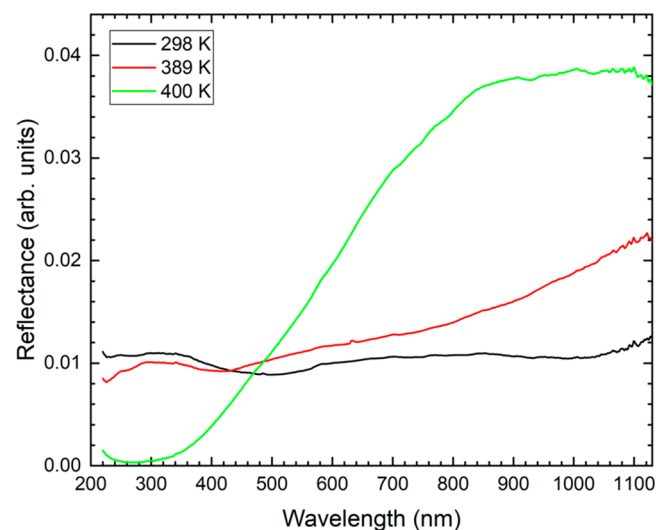
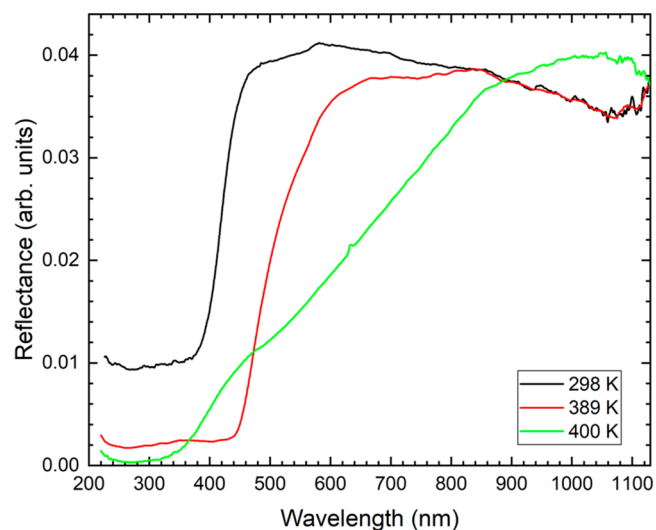


Figure 6. UV–visible spectra of [MAT][DCA] (top) and boron-doped [MAT][DCA] (bottom) levitated in argon as the droplets are heated to successively higher temperatures by the carbon dioxide laser.

Although the uncertainties are large owing to the overlap of peaks b and c, the present measured ratio of 3.3 consequently suggests that the foam is composed of molecules more polymerized than melamine.

The XPS spectrum of the [MAT][DCA] foam in the C(1s) spectral region and the individual peaks fits labeled d–g are shown in Figure 8. The binding energies and relative areas for peaks d–g are presented in Table 4. As evident in Scheme 2, there is only one chemical environment for the carbon atoms in melamine, in which the carbon has two single bonds and one double bond with the nitrogen atoms, N₂=C=N. The C(1s) XPS spectrum of melamine in ref 53 has two main peaks at 284.6 and 287.9 eV, which are assigned to adventitious carbon and the N₂=C=N chemical state, respectively. The so-called “adventitious carbon” refers to the carbonaceous adsorbates that deposit onto a sample when exposed to the atmosphere. In support of the assignment by Dementjev et al.⁵³ for the 287.9 eV peak, Ronning et al.⁵⁵ predict a single emission line for β -C₃N₄ at approximately 288 eV in the C(1s) spectrum produced by the N₂=C=N chemical state. The

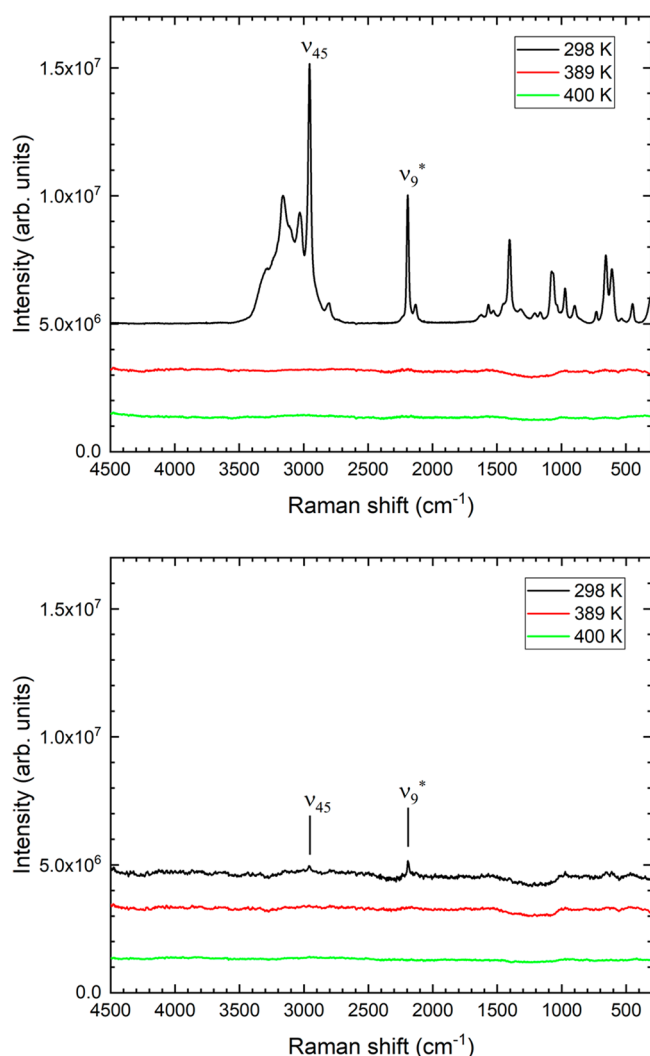


Figure 7. Raman spectra of [MAT][DCA] (top) and boron-doped [MAT][DCA] (bottom) levitated in argon as the droplet is heated to successively higher temperatures by the carbon dioxide laser. The spectrum of pure [MAT][DCA] at 298 K has been displaced vertically for clarity. The ν_{45} and ν_{9^*} peaks for boron-doped [MAT][DCA] can be discerned above the continuum produced by the boron (see ref 28 for the vibrational mode assignments of [MAT][DCA]).

binding energy for adventitious carbon has recently been revised upward to 284.8 eV.⁴⁰ Thus, we assign peaks e and g at the binding energies of 288.1 and 285.2 eV to the $N_2=C=N$ chemical state and adventitious carbon, respectively. Peak f at 286.7 eV is tentatively assigned to the $N-C\equiv N$ chemical state of dicyanamide.²⁷ Finally, the very small peak d at approximately 294 eV, which is also present in melamine, is attributed to π -excitation of the $C=N$ bond.⁵³

In summary, the $N(1s)$ and $C(1s)$ XPS measurements suggest that the nitrogen and carbon atoms occupy essentially the same chemical states in the foam and melamine, namely, $C=N-C$, $C-N=H_2$, and $N_2=C=N$. However, in the $N(1s)$ spectral region, the ratio of the $C=N-C$ to $C-N=H_2$ peak areas in the present measurements at 3.3 ± 1.8 suggests that the foam is more polymerized than melamine (see Scheme 2).

3.2.5. Elemental Analysis of the [MAT][DCA] Foam. The molar ratios N/C, N/H, and C/H for the [MAT][DCA] foam,

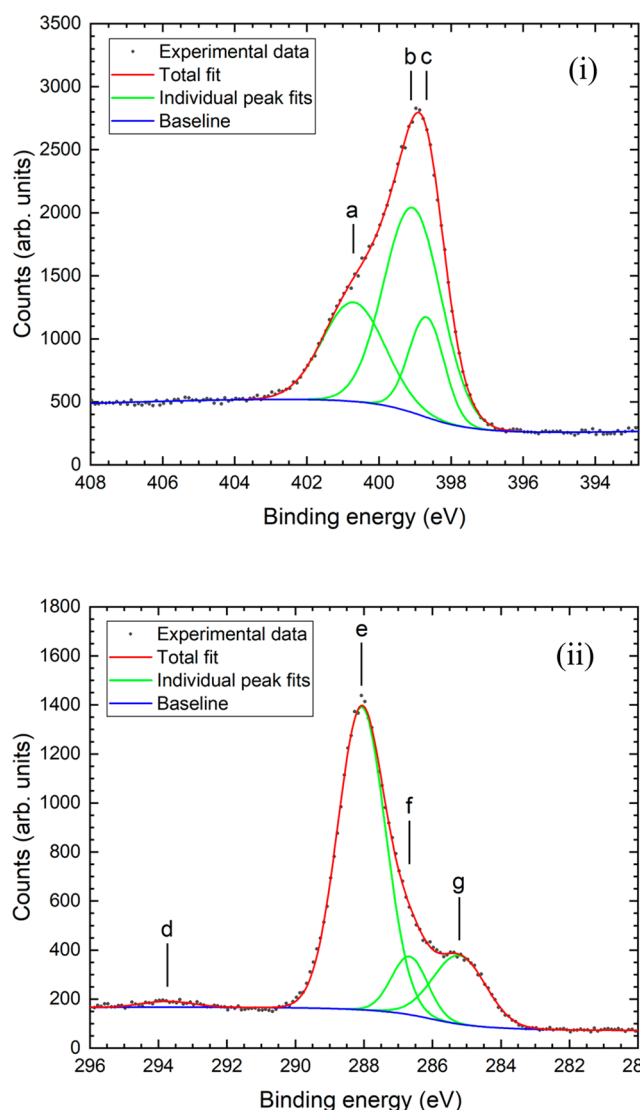


Figure 8. X-ray photoelectron spectra of the [MAT][DCA] foam in the (i) $N(1s)$ and (ii) $C(1s)$ spectral regions. The assignments for the peaks labeled a–g are presented in Table 4.

with and without boron nanoparticles, are presented in Table 5. Repeated measurements of the molar ratio N/C for different [MAT][DCA] foam samples gave consistent results in the range from approximately 1.43 to 1.46, whereas the molar ratios involving hydrogen, namely, N/H and C/H, varied by factors of up to nearly 2. The larger variations in N/H and C/H are probably a consequence of the absorption of different quantities of water by the sample. When using elemental analysis to determine the composition of the foam, we therefore only consider the molar ratio, N/C. The N/C molar ratios for melamine, melam, melem, melon, and graphitic carbon nitride are 2, 1.83, 1.67, 1.5, and 1.33, respectively. The N/C molar ratios of 1.43 and 1.46 for the [MAT][DCA] foam with and without boron nanoparticles, respectively, consequently indicate that the foam is in a condensed form of the polymer such as melon or some combination of condensates with low N/C ratios.

3.3. In Situ Near-Infrared Absorption Spectroscopy of an [MAT][DCA] Droplet. The near-infrared absorption spectra in the $2400\text{--}8000\text{ cm}^{-1}$ spectral region of an [MAT][DCA] droplet levitated in argon are shown in Figure

Table 4. Binding Energies, Relative Areas, And Assignments for the Peaks in the X-ray Photoelectron Spectra (XPS) of the [MAT][DCA] Foam in the N(1s) and C(1s) Spectral Regions

peak label ^a	[MAT][DCA] foam binding energy (eV) ^b (relative area)	reference substance binding energy (eV) ^c	assignment ^c
a	400.7 ± 0.2 (1710 ± 470)	melamine ⁵³ 400.7	N(1s) 
b	399.1 ± 0.2 (3240 ± 250)	melamine ⁵³ 399.1 carbon nitride ⁵⁵ 400	N(1s) C=N-C
c	398.7 ± 0.1 (970 ± 510)	melamine ⁵³ 398.5	N(1s) 
d	293.7 ± 0.2 (44 ± 15)	melamine ⁵³ ≈ 294 eV	C(1s) π-excitation of C=N bond
e	288.1 ± 0.1 (2151 ± 47)	melamine ⁵³ 287.9 carbon nitride ⁵⁵ 288	C(1s) 
f	286.7 ± 0.1 (310 ± 52)	dicyanamide ²⁷ 286.9	C(1s) N-C≡N
g	285.2 ± 0.1 (538 ± 94)	melamine ⁵³ 284.6 pure carbon ⁴⁰ 284.8	C(1s) adventitious carbon

^aa–g correspond to the peak labels in Figure 8. ^bThe quoted errors combine the uncertainties from determining the peak wavenumbers in the fitting procedure and calibrating the wavenumber scale. The uncertainties are equal to, or less than, 1 cm⁻¹ unless stated otherwise. ^cThe assignments were performed by comparison with XPS studies of melamine,⁵³ carbon nitride (β-C₃N₄),⁵⁵ dicyanamide,²⁷ and pure carbon.⁴⁰

Table 5. Molar Ratios N/C, N/H, and C/H for the [MAT][DCA] Foam, with and without Boron Nanoparticles, Determined by Combustion Methodology

elements	molar ratio [MAT][DCA] foam	molar ratio [MAT][DCA] + B foam
N/C	1.434 ± 0.008	1.462 ± 0.008
N/H	2.32 ± 0.01	1.321 ± 0.007
C/H	1.615 ± 0.009	0.903 ± 0.005

9. As the droplet is heated to successively higher temperatures, the observable structure reduces in amplitude and no significant spectral changes are observed before the resonant structure becomes hidden by oscillations produced by the scattering. The reduction in the amplitudes of the peaks suggests that the [MAT][DCA] is decomposing because of the heating. After formation of the foam, a large, broad structure appears in the region from approximately 2500 to 3600 cm⁻¹,

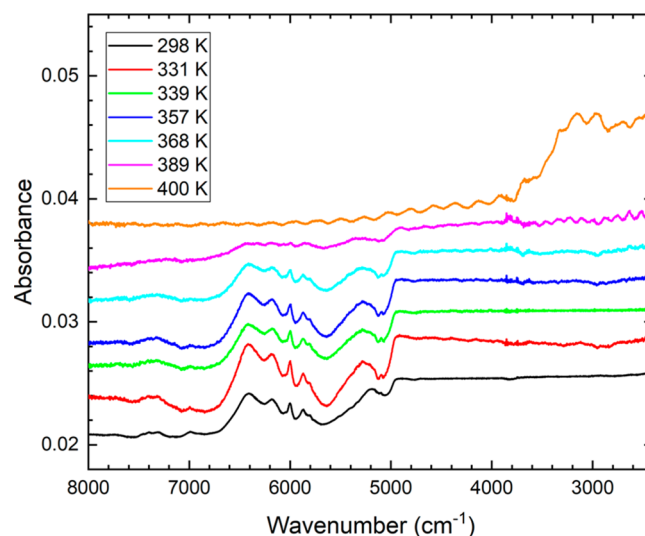


Figure 9. Near-infrared absorption spectra of [MAT][DCA] levitated in argon as the droplet is heated to successively higher temperatures by the carbon dioxide laser. Except for the 298 K data, the spectra have been displaced vertically for comparison purposes. The spectrum of the foam formed at 400 K has also been scaled by the factor of 0.25.

which corresponds to the similar structure observed in the infrared spectrum (Figure 5). In Figure 10, the individual peak

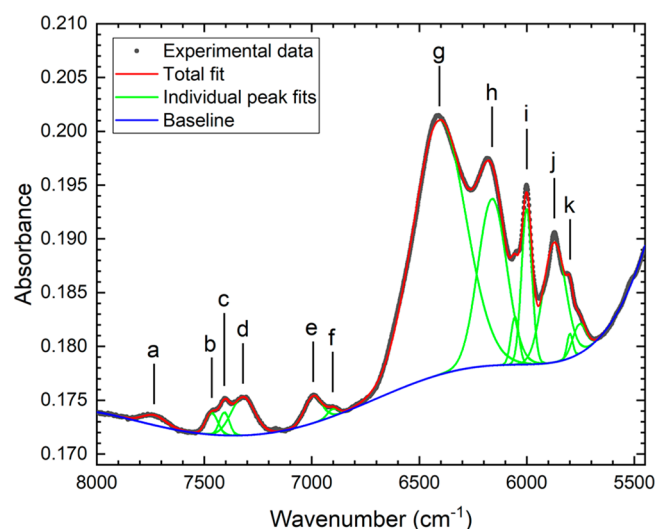


Figure 10. Individual peak fits for an [MAT][DCA] droplet at 298 K in the region of the near-infrared absorption spectrum not significantly distorted by scattering effects. The vibrational assignments for the peaks labeled a to k are presented in Table S1.

fits are shown for the unheated [MAT][DCA] droplet at 298 K in the 5500 to 8000 cm⁻¹ spectral region, where the spectrum is not significantly distorted by scattering effects and consequently the peaks are symmetric. The fundamental modes of [MAT][DCA] occur at wavenumbers below approximately 3500 cm⁻¹ and have significantly higher absorption cross sections than the combination bands and overtones.²⁸ It is therefore remarkable that no structure is observed from 2400 to 3500 cm⁻¹, whereas relatively large symmetric peaks occur in the region from 5700 to 7900 cm⁻¹. As a possible explanation, we note that if the refractive index, *n*, were to reduce to *n* ≈ 1.0 between 5700 and 7900 cm⁻¹, then

the near-infrared beam would pass through the droplet without being significantly deflected or phase-shifted and, hence, reach the detector to record undistorted symmetric absorption lines. The peaks between 5700 and 7900 cm^{-1} may then be interpreted as the combination bands or overtones of the large fundamental modes of [MAT][DCA] below approximately 3500 cm^{-1} . In contrast, if $n > 1$ in the wavenumber region of the fundamental modes, as is typical for ionic liquids,⁵⁶ then the infrared beam would be refracted or deflected before reaching the detector so that no absorption peaks would be recorded. The large, rapid reduction in the absorbance as the wavenumber increases above 5000 cm^{-1} is consistent with a decrease in the refractive index toward one. The wavenumbers and possible vibrational mode assignments for peaks a–k in Figure 10 are presented in Table S1 of the Supporting Information.

4. CONCLUSION

An [MAT][DCA] droplet levitated in argon was heated to increasingly higher temperatures by a carbon dioxide laser, and the resulting temperatures were measured by an IR thermal imaging camera. At each temperature, Fourier-transform infrared, Fourier-transform near-infrared, and UV–visible spectra were recorded. The droplet became increasingly yellow before exploding at 400 K to form a brown foam-like substance and filling the process chamber with a dense smoke. The foam was also studied *ex situ* by X-ray photoelectron spectroscopy, infrared diffuse-reflectance spectroscopy, and elemental analysis.

As a guide to interpret the infrared diffuse-reflectance spectrum of the foam, we first analyzed the infrared diffuse-reflectance spectrum of melamine. The fundamental modes of our melamine sample were assigned by comparison with infrared absorption measurements and calculations for crystalline melamine by Yuan et al.⁴³ The correspondence between the present peak wavenumbers and the values in ref 43 permitted assignments of our melamine vibrational modes in most spectral regions. The similarity of the wavenumbers for many of the peaks in the foam and melamine spectra suggests that these two compounds share the same functional groups and vibrational modes. Several minor features in the [MAT][DCA] foam spectrum not present in melamine were assigned to *small* quantities of unreacted [MAT][DCA].²⁸

The *in situ* infrared absorption spectrum of the smoke produced following formation of the foam was significantly distorted by the scattering of the infrared beam from the smoke particles, and so included asymmetric lineshapes and an oscillatory baseline.^{48,49} However, by accounting for both nonresonant and resonant Mie scattering, we analyzed some spectral regions and thereby showed that the foam and smoke are probably the same substance.

XPS spectra of the foam were recorded in the N(1s) and C(1s) spectral regions. The resulting spectra are different from the corresponding XPS spectra of [MAT][DCA],²⁷ which suggests that [MAT][DCA] is not the *main* component of the foam. In contrast, the N(1s) and C(1s) XPS measurements indicate that the nitrogen and carbon atoms occupy essentially the same chemical states in the foam and melamine.⁵³ Comparison of the peak areas corresponding to the C=N–C and C–N=H₂ chemical states implies, however, that the foam is more polymerized than melamine.

We determined the molar ratios N/C, N/H, and C/H for the [MAT][DCA] foam, with and without boron nano-

particles, by combustion methodology. The N/C molar ratios of 1.43 and 1.46 for the [MAT][DCA] foam with and without boron nanoparticles, respectively, confirm that the foam is in a more condensed form than melamine such as melon or possibly a combination of melamine condensates with lower N/C ratios.

For the *in situ* UV–visible spectra from 200 to 1100 nm, heating caused the absorption in the UV spectral region to increase relative to that in the optical and near-infrared ranges, and the absorption maximum to extend to longer wavelengths. The UV–visible spectra therefore imply that the heating produced an increase in the number of conjugated double bonds, which is consistent with polymerization. For Raman spectroscopy, the heating produced large fluorescent backgrounds and caused the peaks to vanish, so that no information could be extracted about possible chemical changes.

For the *in situ* near-infrared absorption spectrum of the levitated [MAT][DCA] droplet before heating, no structure is observed from 2400 to 3500 cm^{-1} in the region of the fundamental modes but, remarkably, relatively large symmetric peaks occur in the region from 5700 to 7900 cm^{-1} . The phenomena could occur if the refractive index n were to reduce to $n \approx 1.0$ between 5700 and 7900 cm^{-1} , for then the IR beam would pass through the droplet without being significantly deflected or phase shifted and, hence, reach the detector to record symmetric absorption lines. The peaks were consequently assigned to combination bands and overtones of the fundamental modes with large absorption cross sections occurring at lower wavenumbers.²⁸

By using thermogravimetric analysis, Perez et al.²⁷ determined that [MAT][DCA] undergoes a rapid mass loss of 53% at 466 K to leave a polymer derived from [DCA][−]. In contrast, in the present measurements the droplet exploded to form the foam at the lower temperature of 400 K. The formation of the foam was preceded by a period of extremely violent agitation and oscillation of the droplet. A possible explanation for the lower polymerization temperature here is consequently that the explosion was initiated by impact and friction in addition to the heating.

Chingin et al.¹⁶ found that approximately 25% of the [DCA]-containing IL was transformed into a precipitate following reaction with white-fuming nitric acid (HNO₃), whereas Perez et al. observed a rapid mass loss of 53% following the polymerization when [MAT][DCA] was heated in oxygen. Similarly, we found that at least $37 \pm 3\%$ of liquid [MAT][DCA] was transformed into the foam by pyrolysis in the inert gas, Ar. The formation of such stable, solid-state residues clearly represents a serious disadvantage for the application of ionic-liquid-based hypergolic fuels in rocket engines.^{16–18}

In contrast to [MAT][DCA], we found that [BMIM][DCA] does not explode to form the brown foam at 400 K or even at higher temperatures of up to 433 K. Elimination of the amino group (–NH₂) from the [MAT]⁺ cation or the increased energy density provided by the additional nitrogen atom in the triazolium ring (Scheme 1) therefore appear to be essential requirements for the formation of the foam. The present results are consistent with previous findings that ammonia¹⁶ or the amines²⁶ are required to initiate the polymerization of [DCA]-containing ILs.

Regarding the effects of the boron, the foam was formed at approximately 400 K with and without the boron nanoparticles. Furthermore, the only spectroscopic effects of the

boron were, first, to cause the region of high absorption in the UV–visible spectrum to extend across the full wavelength range and, second, to produce a large, structureless continuum in the Raman spectrum. Thus, at the temperatures studied of up to 433 K and for levitation in the inert argon gas, the boron does not produce any significant, observable chemical or physical effects.

■ ASSOCIATED CONTENT

Supporting Information

The Supporting Information is available free of charge on the ACS Publications website at DOI: 10.1021/acs.jpca.8b08993.

Wavenumbers and possible vibrational mode assignments for the peaks in the near-infrared absorption spectrum from 8000 cm^{-1} to 5500 cm^{-1} produced by an [MAT][DCA] droplet levitated in argon (PDF)

■ AUTHOR INFORMATION

Corresponding Author

*E-mail: ralfk@hawaii.edu.

ORCID

Ralf I. Kaiser: 0000-0002-7233-7206

Notes

The authors declare no competing financial interest.

■ ACKNOWLEDGMENTS

This work was supported by the Office of Naval Research under Grant N00014-16-1-2078 (Hawaii).

■ REFERENCES

- Cardulla, F. Hydrazine. *J. Chem. Educ.* **1983**, *60*, 505–508.
- Clark, J. D. *Ignition! An informal history of liquid rocket propellants*; Rutgers University Press: New Brunswick, NJ, 1972; p xiv, 214 pp.
- Schneider, S.; Hawkins, T.; Rosander, M.; Vaghjiani, G.; Chambreau, S.; Drake, G. Ionic liquids as hypergolic fuels. *Energy Fuels* **2008**, *22*, 2871–2872.
- Zhang, Y. Q.; Gao, H. X.; Joo, Y. H.; Shreeve, J. M. Ionic liquids as hypergolic fuels. *Angew. Chem., Int. Ed.* **2011**, *50*, 9554–9562.
- Schneider, S.; Hawkins, T.; Ahmed, Y.; Rosander, M.; Hudgens, L.; Mills, J. Green bipropellants: Hydrogen-rich ionic liquids that are hypergolic with hydrogen peroxide. *Angew. Chem., Int. Ed.* **2011**, *50*, 5886–5888.
- Zhang, Y. Q.; Shreeve, J. M. Dicyanoborate-based ionic liquids as hypergolic fluids. *Angew. Chem., Int. Ed.* **2011**, *50*, 935–937.
- McCrary, P. D.; Chatel, G.; Alaniz, S. A.; Cojocar, O. A.; Beasley, P. A.; Flores, L. A.; Kelley, S. P.; Barber, P. S.; Rogers, R. D. Evaluating ionic liquids as hypergolic fuels: Exploring reactivity from molecular structure. *Energy Fuels* **2014**, *28*, 3460–3473.
- Chambreau, S. D.; Koh, C. J.; Popolan-Vaida, D. M.; Gallegos, C. J.; Hooper, J. B.; Bedrov, D.; Vaghjiani, G. L.; Leone, S. R. Flow-tube investigations of hypergolic reactions of a dicyanamide ionic liquid via tunable vacuum ultraviolet aerosol mass spectrometry. *J. Phys. Chem. A* **2016**, *120*, 8011–8023.
- Welton, T. Room-temperature ionic liquids. Solvents for synthesis and catalysis. *Chem. Rev.* **1999**, *99*, 2071–2083.
- Endres, F.; El Abedin, S. Z. Air and water stable ionic liquids in physical chemistry. *Phys. Chem. Chem. Phys.* **2006**, *8*, 2101–2116.
- Freemantle, M. *An introduction to ionic liquids*; RSC Pub.: Cambridge, U.K., 2010; p xiv, 281 pp.
- Xue, H.; Gao, Y.; Twamley, B.; Shreeve, J. M. New energetic salts based on nitrogen-containing heterocycles. *Chem. Mater.* **2005**, *17*, 191–198.
- Chambreau, S. D.; Schneider, S.; Rosander, M.; Hawkins, T.; Gallegos, C. J.; Pastewait, M. F.; Vaghjiani, G. L. Fourier transform infrared studies in hypergolic ignition of ionic liquids. *J. Phys. Chem. A* **2008**, *112*, 7816–7824.
- Zhang, Q. H.; Shreeve, J. M. Energetic ionic liquids as explosives and propellant fuels: A new journey of ionic liquid chemistry. *Chem. Rev.* **2014**, *114*, 10527–10574.
- Visser, A. E.; Swatloski, R. P.; Reichert, W. M.; Mayton, R.; Sheff, S.; Wierzbicki, A.; Davis, J. H.; Rogers, R. D. Task-specific ionic liquids incorporating novel cations for the coordination and extraction of Hg^{2+} and Cd^{2+} : Synthesis, characterization, and extraction studies. *Environ. Sci. Technol.* **2002**, *36*, 2523–2529.
- Chingin, K.; Perry, R. H.; Chambreau, S. D.; Vaghjiani, G. L.; Zare, R. N. Generation of melamine polymer condensates upon hypergolic ignition of dicyanamide ionic liquids. *Angew. Chem., Int. Ed.* **2011**, *50*, 8634–8637.
- Stoner, C. E.; Brill, T. B. Thermal-decomposition of energetic materials. 46. The formation of melamine-like cyclic azines as a mechanism for ballistic modification of composite propellants by DCD, DAG, and DAF. *Combust. Flame* **1991**, *83*, 302–308.
- Williams, G. K.; Palopoli, S. F.; Brill, T. B. Thermal decomposition of energetic materials. 65. Conversion of insensitive explosives (NTO, ANTA) and related compounds to polymeric melon-like cyclic azine burn-rate suppressants. *Combust. Flame* **1994**, *98*, 197–204.
- Jurgens, B.; Hoppe, H. A.; Irran, E.; Schnick, W. Transformation of ammonium dicyanamide into Dicyandiamide in the solid. *Inorg. Chem.* **2002**, *41*, 4849–4851.
- Lotsch, B. V.; Schnick, W. Towards novel C-N materials: crystal structures of two polymorphs of guanidinium dicyanamide and their thermal conversion into melamine. *New J. Chem.* **2004**, *28*, 1129–1136.
- Costa, L.; Camino, G. Thermal behaviour of melamine. *J. Therm. Anal.* **1988**, *34*, 423–429.
- Lotsch, B. V.; Schnick, W. New light on an old story: Formation of melam during thermal condensation of melamine. *Chem. - Eur. J.* **2007**, *13*, 4956–4968.
- Jurgens, B.; Irran, E.; Senker, J.; Kroll, P.; Muller, H.; Schnick, W. Melem (2,5,8-triamino-tri-s-triazine), an important intermediate during condensation of melamine rings to graphitic carbon nitride: Synthesis, structure determination by X-ray powder diffraction, solid-state NMR, and theoretical studies. *J. Am. Chem. Soc.* **2003**, *125*, 10288–10300.
- Sattler, A.; Pagano, S.; Zeuner, M.; Zurawski, A.; Gunzelmann, D.; Senker, J.; Muller-Buschbaum, K.; Schnick, W. Melamine-melem adduct phases: Investigating the thermal condensation of melamine. *Chem. - Eur. J.* **2009**, *15*, 13161–13170.
- Paraknowitsch, J. P.; Zhang, J.; Su, D. S.; Thomas, A.; Antonietti, M. Ionic liquids as precursors for nitrogen-doped graphitic carbon. *Adv. Mater.* **2010**, *22*, 87–92.
- Wooster, T. J.; Johanson, K. M.; Fraser, K. J.; MacFarlane, D. R.; Scott, J. L. Thermal degradation of cyano containing ionic liquids. *Green Chem.* **2006**, *8*, 691–696.
- Perez, J. P. L.; McMahan, B. W.; Schneider, S.; Boatz, J. A.; Hawkins, T. W.; McCrary, P. D.; Beasley, P. A.; Kelley, S. P.; Rogers, R. D.; Anderson, S. L. Exploring the structure of nitrogen-rich ionic liquids and their binding to the surface of oxide-free boron nanoparticles. *J. Phys. Chem. C* **2013**, *117*, 5693–5707.
- Brotton, S. J.; Lucas, M.; Chambreau, S. D.; Vaghjiani, G. L.; Yu, J.; Anderson, S. L.; Kaiser, R. I. Spectroscopic investigation of the primary reaction intermediates in the oxidation of levitated droplets of energetic ionic liquids. *J. Phys. Chem. Lett.* **2017**, *8*, 6053–6059.
- Brotton, S. J.; Lucas, M.; Jensen, T. N.; Anderson, S. L.; Kaiser, R. I. A spectroscopic study on the intermediates and reaction rates in the oxidation of levitated droplets of energetic ionic liquids by nitrogen dioxide. *J. Phys. Chem. A* **2018**, *122*, 7351–7377.
- Brotton, S. J.; Kaiser, R. I. Novel high-temperature and pressure-compatible ultrasonic levitator apparatus coupled to Raman and Fourier transform infrared spectrometers. *Rev. Sci. Instrum.* **2013**, *84*, 055114.

- (31) Brotton, S. J.; Kaiser, R. I. In situ Raman spectroscopic study of gypsum ($\text{CaSO}_4 \cdot 2\text{H}_2\text{O}$) and epsomite ($\text{MgSO}_4 \cdot 7\text{H}_2\text{O}$) dehydration utilizing an ultrasonic levitator. *J. Phys. Chem. Lett.* **2013**, *4*, 669–673.
- (32) McCrary, P. D.; Beasley, P. A.; Cojocaru, O. A.; Schneider, S.; Hawkins, T. W.; Perez, J. P. L.; McMahon, B. W.; Pfeil, M.; Boatz, J. A.; Anderson, S. L.; et al. Hypergolic ionic liquids to mill, suspend, and ignite boron nanoparticles. *Chem. Commun.* **2012**, *48*, 4311–4313.
- (33) Liu, A. Y.; Cohen, M. L. Prediction of new low compressibility solids. *Science* **1989**, *245*, 841–842.
- (34) Niu, C. M.; Lu, Y. Z.; Lieber, C. M. Experimental realization of the covalent solid carbon nitride. *Science* **1993**, *261*, 334–337.
- (35) Yin, L. W.; Bando, Y.; Li, M. S.; Liu, Y. X.; Qi, Y. X. Unique single-crystalline beta carbon nitride nanorods. *Adv. Mater.* **2003**, *15*, 1840–1844.
- (36) MartinGil, J.; MartinGil, F. J.; Sarikaya, M.; Qian, M. X.; JoseYacaman, M.; Rubio, A. Evidence of a low compressibility carbon nitride with defect-zincblende structure. *J. Appl. Phys.* **1997**, *81*, 2555–2559.
- (37) Xie, W. J.; Wei, B. Parametric study of single-axis acoustic levitation. *Appl. Phys. Lett.* **2001**, *79*, 881–883.
- (38) Bennett, C. J.; Brotton, S. J.; Jones, B. M.; Misra, A. K.; Sharma, S. K.; Kaiser, R. I. High-sensitivity Raman spectrometer to study pristine and irradiated interstellar ice analogs. *Anal. Chem.* **2013**, *85*, 5659–5665.
- (39) Kortüm, G. *Reflectance spectroscopy. Principles, methods, applications*; Springer: Berlin, Heidelberg, New York, 1969; p vi, 366 pp.
- (40) NIST. *X-ray photoelectron spectroscopy database, NIST standard reference database number 20*. <https://srdata.nist.gov/xps/>, National Institute of Standards and Technology: Gaithersburg, MD, 2000; DOI: 10.18434/T4T88K.
- (41) Hawkins, T. W.; Schneider, S.; Drake, G. W.; Vaghjiani, G.; Chambreau, S. Hypergolic fuels containing fuel and oxidizer for liquid rockets or propellants. U.S. Patent 8034202B1, 2011.
- (42) Perez, J. P. L.; Yu, J.; Sheppard, A. J.; Chambreau, S. D.; Vaghjiani, G. L.; Anderson, S. L. Binding of alkenes and ionic liquids to B-H-functionalized boron nanoparticles: Creation of particles with controlled dispersibility and minimal surface oxidation. *ACS Appl. Mater. Interfaces* **2015**, *7*, 9991–10003.
- (43) Yuan, X. H.; Luo, K.; Zhang, K. Q.; He, J. L.; Zhao, Y. C.; Yu, D. L. Combinatorial vibration-mode assignment for the FTIR spectrum of crystalline melamine: A strategic approach toward theoretical IR vibrational calculations of triazine-based compounds. *J. Phys. Chem. A* **2016**, *120*, 7427–7433.
- (44) Wang, Y. L.; Mebel, A. M.; Wu, C. J.; Chen, Y. T.; Lin, C. E.; Jiang, J. C. IR spectroscopy and theoretical vibrational calculation of the melamine molecule. *J. Chem. Soc., Faraday Trans.* **1997**, *93*, 3445–3451.
- (45) Mircescu, N. E.; Oltean, M.; Chis, V.; Leopold, N. FTIR, FT-Raman, SERS and DFT study on melamine. *Vib. Spectrosc.* **2012**, *62*, 165–171.
- (46) Paschoal, V. H.; Faria, L. F. O.; Ribeiro, M. C. C. Vibrational spectroscopy of ionic liquids. *Chem. Rev.* **2017**, *117*, 7053–7112.
- (47) Kiefer, J.; Noack, K.; Penna, T. C.; Ribeiro, M. C. C.; Weber, H.; Kirchner, B. Vibrational signatures of anionic cyano groups in imidazolium ionic liquids. *Vib. Spectrosc.* **2017**, *91*, 141–146.
- (48) Bohren, C. F.; Huffman, D. R. *Absorption and scattering of light by small particles*; Wiley: New York, 1983; p xiv, 530 pp.
- (49) Bassan, P.; Byrne, H. J.; Bonnier, F.; Lee, J.; Dumas, P.; Gardner, P. Resonant Mie scattering in infrared spectroscopy of biological materials - understanding the 'dispersion artefact'. *Analyst* **2009**, *134*, 1586–1593.
- (50) Shore, B. W. Scattering theory of absorption-line profiles and refractivity. *Rev. Mod. Phys.* **1967**, *39*, 439–462.
- (51) Rätty, J.; Peiponen, K. E.; Asakura, T. *UV-visible reflection spectroscopy of liquids*; Springer: Berlin, New York, 2004; p xii, 221 pp.
- (52) Brotton, S. J.; Shapiro, R.; van der Laan, G.; Guo, J.; Glans, P. A.; Ajello, J. M. Valence state fossils in Proterozoic stromatolites by L-edge X-ray absorption spectroscopy. *J. Geophys. Res.-Biogeosci.* **2007**, *112*, G03004.
- (53) Dementjev, A. P.; de Graaf, A.; van de Sanden, M. C. M.; Maslakov, K. I.; Naumkin, A. V.; Serov, A. A. X-ray photoelectron spectroscopy reference data for identification of the C_3N_4 phase in carbon-nitrogen films. *Diamond Relat. Mater.* **2000**, *9*, 1904–1907.
- (54) Siegbahn, K.; Uppsala, K. V.-s. i. ESCA; *atomic, molecular and solid state structure studied by means of electron spectroscopy*; Almqvist & Wiksells: Uppsala, 1967; p 283.
- (55) Ronning, C.; Feldermann, H.; Merk, R.; Hofsass, H.; Reinke, P.; Thiele, J. U. Carbon nitride deposited using energetic species: A review on XPS studies. *Phys. Rev. B: Condens. Matter Mater. Phys.* **1998**, *58*, 2207–2215.
- (56) Seoane, R. G.; Corderi, S.; Gomez, E.; Calvar, N.; Gonzalez, E. J.; Macedo, E. A.; Dominguez, A. Temperature dependence and structural influence on the thermophysical properties of eleven commercial ionic liquids. *Ind. Eng. Chem. Res.* **2012**, *51*, 2492–2504.